Journal of
Marine Science and Engineering

MDPI

Article

Numerical Study on Internal and External Flow Fields of the UHMWPE Cage

Yiyang Hu [1,2,3], Haisheng Zhao [1,2,3,*], Wei Shi [1,3], Chunwei Bi [4] and Xin Li [1,2,3,*]

1 State Key Laboratory of Coastal and Offshore Engineering, Dalian University of Technology, Dalian 116024, China; huyy22106176@mail.dlut.edu.cn (Y.H.); weishi@dlut.edu.cn (W.S.)
2 School of Hydraulic Engineering, Faculty of Infrastructure Engineering, Dalian University of Technology, Dalian 116024, China
3 Ningbo Institute, Dalian University of Technology, Ningbo 315032, China
4 Fisheries College, Ocean University of China, Qingdao 266100, China; bichunwei@ouc.edu.cn
* Correspondence: hzhao@dlut.edu.cn (H.Z.); lixin@dlut.edu.cn (X.L.)

Abstract: Ultra-high molecular weight polyethylene (UHMWPE) is a new kind of fishing gear material applied in deep-sea fishing cages, which is becoming a trend. Studies on the internal and external flow fields of cages made of UHMWPE have been scarce previously. Therefore, a three-dimensional numerical model for the UHMWPE cage is established herein, where the cage is modeled by a porous media model. The Darcy–Forchheimer coefficients of the porous media are obtained by physical model experiments and numerical simulations. Then, the cylindrical cage is divided into 16 planar nets circumferentially, along with an additional bottom net, to investigate its internal and external flow fields numerically. For a single cylindrical cage, the degree of deceleration decreases as the flow velocity increases, and this effect becomes less apparent when the flow velocity reaches a certain threshold. Finally, the flow field characteristics of double cages with different spacing and multiple cages with equal spacing are revealed.

Keywords: aquaculture cage; porous media model; numerical simulation; flow field

check for updates

Citation: Hu, Y.; Zhao, H.; Shi, W.; Bi, C.; Li, X. Numerical Study on Internal and External Flow Fields of the UHMWPE Cage. *J. Mar. Sci. Eng.* **2023**, *11*, 1881. https://doi.org/10.3390/jmse11101881

Academic Editor: Nitai Drimer

Received: 5 August 2023
Revised: 19 September 2023
Accepted: 21 September 2023
Published: 27 September 2023

1. Introduction

With the increasing demand for aquatic products, marine fisheries are moving towards mariculture to alleviate pressure from environmental and resource constraints. According to the Food and Agriculture Organization (Rome, Italy), cultivated aquatic species will contribute around 53% of the world's seafood supply by 2030 [1]. Deep-sea cage farming has several advantages over traditional offshore aquaculture, such as low pollution, high quality, high efficiency, and standardization, which can improve food security and reduce poverty globally [2–4]. In the mariculture cage, the water quality and rate of water exchange inside the cage significantly affect the survival environment of cultures, in other words, the quality of seafood is affected by the internal and external flow field characteristics of the cage [5]. Therefore, it is crucial to study the flow field characteristics inside and outside the aquaculture cage to ensure the high quality and reliability of mariculture.

Considering the large size and complex working environment of aquaculture nets, it is necessary to conduct physical model experiments in the flume. A large number of researchers have conducted experiments to consider the hydrodynamic responses of the cage [6–10]. For the simple net structure forming the cage, Tauti [11] studied the hydrodynamic coefficients of planar nets in natural water as early as the 1930s, and later proposed a similarity theory that provided the theoretical basis for the flume experiments. The physical model experiments were carried out to study the velocity reduction and wake characteristics of planar nets made of polyethylene (PE) or polyamide (PA) [12]. Subsequently, Bi et al. [13] investigated the drag and surrounding flow field characteristics of planar nets with different degrees of biofouling in the current. For the overall structures of aquaculture cages, Gansel et al. [14] analyzed the wake and drag force of cylindrical cages with different porosities, and it was found that the drag force decreased with larger porosity. In addition, cylindrical cages with smaller porosity were less permeable; their wakes showed similar characteristics to that of a solid cylinder, viz. vortex streets [15,16]. Zhao et al. [17] analyzed the change in hydrodynamic response and mooring force of various aquaculture cage structures through physical model experiments in the flume. Plew et al. [18] and Bi et al. [19] studied the effect of cultured fish on the internal and external flow field characteristics and hydrodynamic properties of the cage, which provided a reference for relevant full-scale model experiments. Park et al. [20] considered the influence of cultured fish on the flow field around the nets in in situ tests as well, and a pseudo-fish-school structure model was developed; then, based on this model, the drag force acting on the cage and the current velocity inside and around the cage were analyzed. Moreover, some researchers have conducted a series of experiments on full-size real aquaculture cages in specific sea areas to reveal how the flow field and wake characteristics are affected by fish, current, etc. [21,22]. Dong et al. [23] performed both model experiments and full-size net cage experiments to study the drag and deformation of aquaculture cage.

Due to the limitations of physical model experiments, it is not easy to reflect the real working conditions of an aquaculture cage. Hence, numerical calculation is an alternative for representing the flow field characteristics of the cage [7]. Even though a real fishing net is flexible and deformable, the porous media model is widely employed in simulating the fishing cage by assuming it to be rigid due to the negligible effect of the net line on the flow field. Patursson et al. [24] considered the surrounding flow field and the forces on the rigid net based on the porous media model, where the results obtained were basically consistent with the experimental tests. Zhao et al. [25,26] utilized a porous media model to analyze the forces and surrounding flow field under various working conditions in rigid planar nets made of PA, and then the results calculated were applied to cylindrical gravity net cages. Bi et al. [27–29] adopted the porous media model to study the damping effect of rigid PE nets and biologically contaminated nets on waves, and the inside flow field and hydrodynamic properties of PA nets were revealed as well. Chen and Christensen [30,31] introduced a novel approach to calculate the coefficients of porous media based on the Morrison equation; moreover, a flow-solid coupling model was proposed by combining the porous media model with the concentrated mass method to model a flexible net. Recently, Liu et al. [32,33] characterized the flow velocity distribution inside and around a semi-submersible aquaculture platform model with rigid nets by employing the porous media method and rigid wall assumption, and then the developed numerical method was utilized to assess the flow field of a novel rigid net cage incorporating a shielding device.

In summary, researchers have conducted extensive studies on the flow fields and hydrodynamic characteristics of aquaculture cages, while the materials of the cages were almost always PE, PA, or metal, which have limited ability to adapt to the challenging deep-sea environment. To address this issue, an increasing number of new materials are being proposed for mariculture, and ultra-high molecular weight polyethylene (UHMWPE) fiber has emerged as a promising high-performance option for fishing applications due to its superior impact resistance, creep resistance, and wear resistance [34,35]. This material has been adopted for producing cages suitable for use in deep-sea aquaculture facilities, such as “Deep Blue I” and “Long Whale I”. However, to the best of the authors’ knowledge, no previous studies have investigated the internal and external flow field characteristics of cages made from UHMWPE nets via the CFD method. Therefore, the objective of this study is to develop a three-dimensional CFD numerical model using the porous media approach [24,36] to simulate the flow field characteristics of a rigid cage made from UHMWPE net. Firstly, the method of fitting the unknown Darcy–Forchheimer coefficients [24,36] is presented; subsequently, the cylindrical cage model is constructed based on the obtained porous media model, and its internal and external flow field properties are revealed.

2. Theoretical Methods

2.1. Equation of Motion in the Time Domain

In order to obtain the flow field in and around the cage, the fluid in the computational domain is considered incompressible is described by the following Reynolds time-averaged Navier–Stokes (RANS) equation and continuity equation:

$$\frac{\partial(\rho u_i)}{\partial t} + \frac{\partial(\rho u_i u_j)}{\partial x_j} = -\frac{\partial P}{\partial x_i} + \frac{\partial}{\partial x_j}\mu_{eff}\left(\frac{\partial u_i}{\partial x_j} + \frac{\partial u_j}{\partial x_i}\right) + S_i \quad (1)$$

$$\frac{\partial \rho}{\partial t} + \frac{\partial(\rho u_i)}{\partial x_i} = 0 \quad (2)$$

where u_i is the average velocity component in the corresponding direction; x_1, x_2 and x_3 correspond to the x, y, and z directions, respectively; ρ is the density of the fluid; t is the time; $\mu_{eff} = (\mu + \mu_t)$ is the effective dynamic viscosity of the fluid with μ and μ_t being the dynamic viscosity and eddy viscosity, respectively; $\mu_t = \rho C_\mu \frac{k^2}{\varepsilon}$; $C_\mu = 0.09$; k is the turbulent kinetic energy; ε is the turbulent dissipation rate; $P = p + \frac{2}{3}\rho k$, p is pressure; S_i is the source term for the momentum equation.

The realizable $k - \varepsilon$ turbulence model [37] is used to consider the turbulence effect, which has high stability and convergence in describing free fluid with the strong pressure gradient. In view of the blockage effect and permeability of the planar net structure, the realizable $k - \varepsilon$ turbulence model is applied herein. The equations of turbulent kinetic energy k and turbulent dissipation rate ε for the current turbulence model are as follows:

$$\frac{\partial}{\partial t}(\rho k) + \frac{\partial}{\partial x_j}(\rho k u_j) = \frac{\partial}{\partial x_j}\left[\left(\mu + \frac{\mu_t}{\sigma_k}\right)\frac{\partial k}{\partial x_j}\right] + P_k + P_b - \rho\varepsilon - Y_M + S_k \quad (3)$$

$$\frac{\partial}{\partial t}(\rho \varepsilon) + \frac{\partial}{\partial x_j}(\rho \varepsilon u_j) = \frac{\partial}{\partial x_j}\left[\left(\mu + \frac{\mu_t}{\sigma_\varepsilon}\right)\frac{\partial \varepsilon}{\partial x_j}\right] + \rho C_1 S\varepsilon - \rho C_2 \frac{\varepsilon^2}{k + \sqrt{\nu\varepsilon}} + C_{1\varepsilon}\frac{\varepsilon}{k}C_{3\varepsilon}P_b + S_\varepsilon \quad (4)$$

$$C_1 = max\left[0.43, \frac{\eta}{\eta + 5}\right], \ \ \eta = S\frac{k}{\varepsilon}, \ \ S = \sqrt{2S_{ij}S_{ij}}, \ \ S_{ij} = \frac{1}{2}\left(\frac{\partial u_i}{\partial x_j} + \frac{\partial u_j}{\partial x_i}\right) \quad (5)$$

where P_k is the turbulent kinetic energy generated by the average velocity gradient; P_b is the kinetic energy of turbulence generated by buoyancy; Y_M is the correction term of compressibility generated by the fluctuating expansion in compressible turbulence, which represents the contribution of fluctuating expansion in compressible turbulence to the total dissipation rate; S is the modulus of the mean rate-of-strain tensor; σ_k and σ_ε are the turbulent Prandtl numbers of k and ε, respectively; S_k and S_ε are the source terms of k and ε, respectively; $C_{1\varepsilon}$, $C_{2\varepsilon}$, and $C_{3\varepsilon}$ are constants.

Since the fluid is considered to be incompressible and adiabatic, $P_b = 0$, $Y_M = 0$, $S_k = 0$, $S_\varepsilon = 0$. $C_{3\varepsilon}$ is the coefficient related to buoyancy in the calculation of compressible flow, where $C_{3\varepsilon} = 1.0$ when the main flow is parallel to the direction of gravity and $C_{3\varepsilon} = 0$ when perpendicular to the direction of gravity. The constants for the realizable $k - \varepsilon$ turbulence model are $C_{1\varepsilon} = 1.44$, $C_2 = 1.9$, $\sigma_k = 1.0$, $\sigma_\varepsilon = 1.2$.

2.2. The Porous Media Model

The porous media model is a mathematical model describing the flow of fluid in porous media, which complies with the Darcy–Forchheimer law [36]. The mathematical expression of this model actually reflects a pressure gradient. Hence, the fishing net used to form the cage is represented by the porous media model [25,26] to simulate the blockage of it mathematically. A source term S_i, determined by the Darcy–Forchheimer law, is incorporated into the momentum equation as follows:

$$S_i = -\left(\sum_{j=1}^{3} D_{ij}\mu u_j + \sum_{j=1}^{3} C_{ij}\frac{1}{2}\rho|u_j|u_j\right) \tag{6}$$

$$D = \begin{bmatrix} D_n & 0 & 0 \\ 0 & D_t & 0 \\ 0 & 0 & D_t \end{bmatrix}, C = \begin{bmatrix} C_n & 0 & 0 \\ 0 & C_t & 0 \\ 0 & 0 & C_t \end{bmatrix} \tag{7}$$

where D and C are known matrices denoting viscous loss and inertial loss, respectively; subscripts n and t represent the normal and tangential directions, respectively.

With the fluid flowing through the porous media, the hydrodynamic force acting on the porous media is calculated by the following equation:

$$F_i = -S_i\lambda A \tag{8}$$

where λ denotes the thickness of porous media; A is the area of porous media; F_i is the hydrodynamic component acting on the porous medium, whose direction is opposite to the direction of the velocity component of the flow field.

By substituting Equation (6) into Equation (8), the expressions of the drag force F_d and lift force F_l for the net under the current can be obtained:

$$F_d = \left(D_n\mu u_p + \frac{1}{2}C_n\rho|u_p|u_p\right)\lambda A \tag{9}$$

$$F_l = \left(D_t\mu u_p + \frac{1}{2}C_t\rho|u_p|u_p\right)\lambda A \tag{10}$$

where u_p is the flow velocity of water particles in the porous media.

When an angle α exists between the net and the current, as shown in Figure 1, the coordinate transformation is required for the Darcy–Forchheimer coefficient [25]:

$$\begin{cases} D'_n = D'_{11} = \frac{D_n+D_t}{2} - \frac{D_n-D_t}{2}\cos(2\alpha) \\ C'_n = C'_{11} = \frac{C_n+C_t}{2} - \frac{C_n-C_t}{2}\cos(2\alpha) \\ D'_t = D'_{12} = \frac{D_n-D_t}{2}\sin(2\alpha) \\ C'_t = C'_{12} = \frac{C_n-C_t}{2}\sin(2\alpha) \end{cases} \tag{11}$$

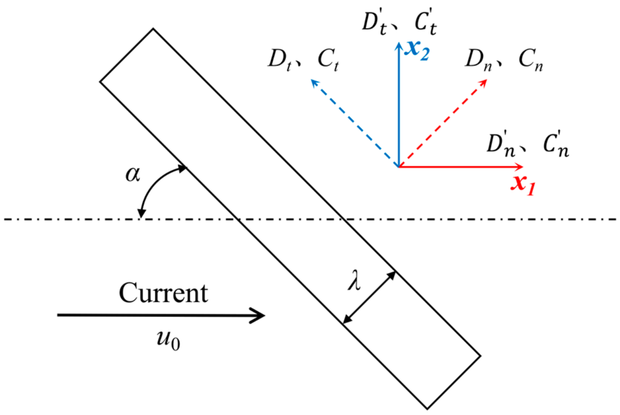

Figure 1. Sketch of the attack angle between the net and the current (λ denotes the thickness of porous media; u_0 is the incoming velocity; α is the angle between the fishing net and the current).

Therefore, the transformed formulas for the drag and lift force are as follows:

$$F_d = \left(D'_n \mu u_p + C'_n \frac{1}{2}\rho |u_p| u_p\right)\lambda A \tag{12}$$

$$F_l = \left(D'_t \mu u_p + C'_t \frac{1}{2}\rho |u_p| u_p\right)\lambda A \tag{13}$$

The ratio between u_p and u_0 is defined as follows:

$$r = \frac{u_p}{u_0} \tag{14}$$

where r is the reduction factor for flow velocity in the porous media; u_0 is the incoming flow velocity.

According to reference [24], the reduction factor for flow velocity in the porous media (r) is determined as follows:

$$r = 1 - r_n C_d \tag{15}$$

where C_d is the drag coefficient of the net; r_n is the flow velocity reduction factor related to α, which are provided in Table 1. The Darcy–Forchheimer coefficient is fitted by an iterative correction method herein instead of the traditional fitting method, due to its large error. In the iterative process, $1 - r_n C_d$ can be adopted as the initial input value of r, and the specific iterative process is described in Section 3.3.

Table 1. The r_n related different attack angles.

$\boldsymbol{\alpha}$	0°	15°	30°	45°	60°	90°
$\boldsymbol{r_n}$	22.8	1.85	0.704	0.395	0.251	0.176

3. Establishing and Validating the Porous Media Model for a Planar Net

3.1. Review for Experiment

In this study, the experimental data used to build the model are obtained from a Master's thesis submitted at Shanghai Ocean University [38], where the width and depth of the experimental flume are 6 m and 2.3 m, respectively. The net is fixed to a frame made of 0.02 m × 0.02 m hollow stainless steel, which is positioned at a center height of 0.47 m from the water surface, and the parameters of the herein net are shown in Table 2. The solidity of the net is calculated by Equation (16), as outlined in the Ph.D. thesis published by [39]:

$$S = \frac{2d}{a} - \left(\frac{d_p}{a}\right)^2 \tag{16}$$

where S is the solidity of the net; d_p is the nominal diameter of the twines; a is the length of the twines. A sketch of the net mesh is presented in Figure 2. During the experiment, seven angles of attack—0°, 15°, 30°, 45°, 60°, 75°, and 90°—as well as five relative flow velocities of the net and the current—0.4 m/s, 0.6 m/s, 0.8 m/s, 1.0 m/s, and 1.2 m/s—are tested, where the cross-combination of these factors results in 35 operating conditions. The schematic diagram of the experimental equipment is shown in Figure 3.

Table 2. Parameters of the UHMWPE planar net used in the experiment.

Line Density of Single Strand	**Number of Strands for Twines**	**T-Meshes**	**N-Meshes**	**Bar Size (a)**
1600 dtex	25	10	10	35 mm
Mesh size	**Nominal diameter of twines (d_p)**	**Length/width of net**	**Density of the UHMWPE material**	**Solidity of net**
70 mm	2.292 mm	0.495 m	970 kg/m^3	0.13

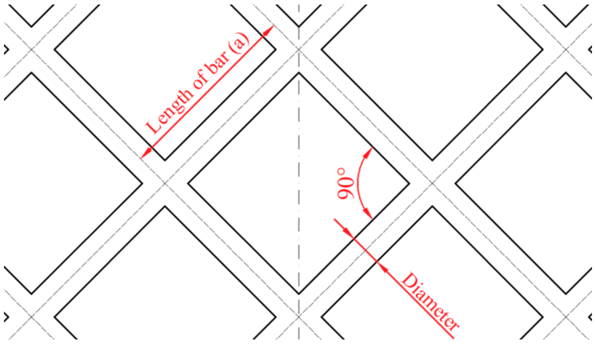

Figure 2. Sketch of the net mesh.

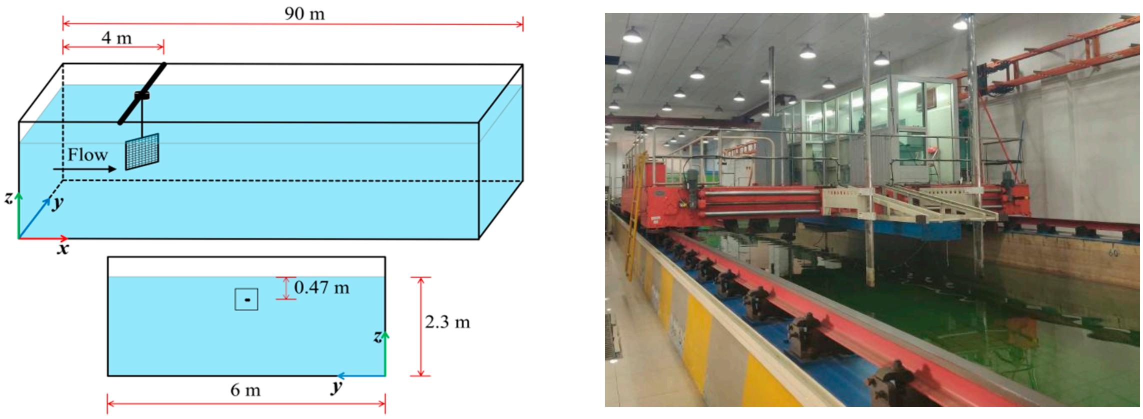

(**a**) (**b**)

Figure 3. Schematic diagram of the experimental equipment. (**a**) Sketch of the experimental equipment (Top figure is a 3-D view of the experimental flume; bottom figure is the side view of the experimental flume). (**b**) Photograph of the experimental equipment [38].

3.2. Establishing a Numerical Model of the Planar Net

3.2.1. Overview of the Numerical Model

The three-dimensional numerical flume used in this study has a height of 2.3 m, a width of 6 m, and a length of 20 m, and is constructed corresponding to the experiment of a planar net through open-source OpenFOAM-v2206 software. The planar net is established using the porous media model with its length and width consistent with the physical model, whose thickness is chosen to be 50 mm herein, without significantly affecting the simulation in previous research [24].

Figure 4 illustrates the numerical flume, depicting boundary conditions used in the simulation, while the frame is described as the no-slip boundary condition, implying that the velocity of the fluid at the boundary is zero. The realizable $k-\varepsilon$ turbulence model is used to simulate the turbulence effect, and the input values of k and ε at the velocity inlet boundary are calculated using Equation (17), while the other boundaries are described by standard wall functions. The input values of k and ε for different velocities are presented in Table 3.

$$I = 0.16 Re_D^{-0.125}\ ;\ k = 1.5\left(\overline{u}l\right)^2\ ;\ \varepsilon = C_u^{3/4}\frac{k^{1.5}}{l} \tag{17}$$

$$Re_D = \frac{\rho u_0 d_p}{\mu} \tag{18}$$

where Re_D is the Reynolds number determined according to the hydraulic diameter of the flume; I is the turbulence intensity; $\overline{u}$ is the turbulence velocity; l is the turbulence length scale; $C_u^{3/4}$ is the empirical constant in the $k-\varepsilon$ model.

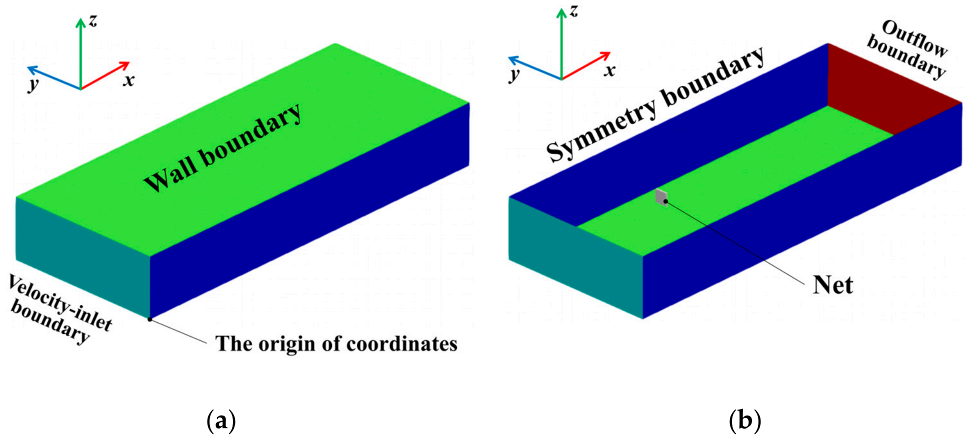

Figure 4. The diagram of the numerical flume of fishing net. (**a**) External view of the numerical flume. (**b**) Internal view of the numerical flume.

Table 3. The input values of k and ε of the numerical model for the planar net.

Velocity (m/s)	k (m^{-2}/s^{-2})	ε (m^{-2}/s^{-3})
0.4	0.000161725	9.27081×10^{-7}
0.6	0.000328804	2.68755×10^{-6}
0.8	0.000543977	5.71901×10^{-6}
1.0	0.000803846	1.02733×10^{-5}
1.2	0.001105962	1.65791×10^{-5}

For this simulation, the simpleFoam solver based on the SIMPLE algorithm is selected to solve the governing equations, where the discretization schemes for pressure, momentum, turbulent kinetic energy and turbulent dissipation rate are adopted using a second-order upwind scheme.

3.2.2. Gridding Mesh and Convergence Analysis

The cell mesh for the numerical flume is generated by the mesh partitioning tool that comes with OpenFOAM software, providing high-quality gridding. The profiles of three directions over the center point of the planar net are shown in Figure 5. The grid level of the basal mesh of the numerical flume and the rectangular area with diagonal vertex coordinates (0, 2, 1.3) and (15, 4, 2.3) are set to 0 and 2, respectively, where the corresponding relationship between the grid level and mesh size is explained in Table 4.

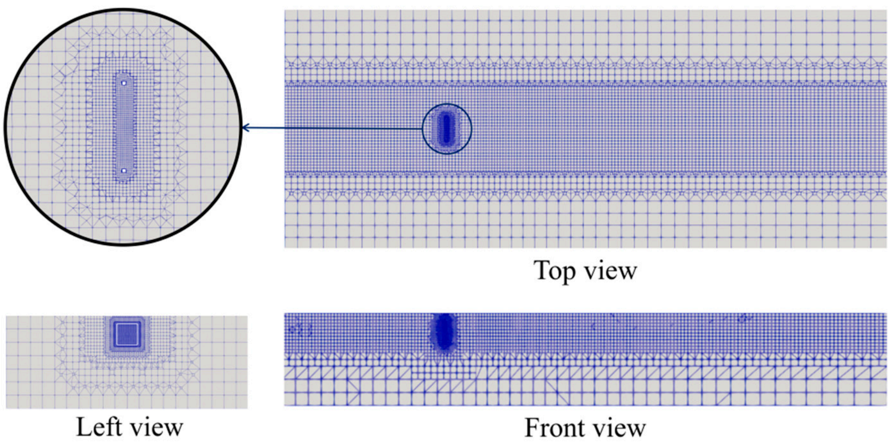

Figure 5. The three views and local schematics of the mesh.

Table 4. Corresponding relationship between the mesh level and mesh size.

Grid Level	0	1	2	3	4	5	6
Mesh size	0.32 m	0.16 m	0.08 m	0.04 m	0.02 m	0.01 m	0.005 m

Convergence analysis of the mesh is crucial for determining the appropriate mesh size that does not affect the simulation results of numerical flume. Hence, three types of mesh with different sizes are proposed, whose grid levels are exhibited in Table 5. Subsequently, the accuracy of the mesh is evaluated by comparing the C_d and C_l obtained from the simulation and experiment. Figure 6a illustrates the comparison of the three meshes, where the Medium gridding method is finally selected for subsequent simulations due to its small number of meshes and the minimal difference in results compared to the Fine gridding method. Then, the Medium gridding method is applied to the numerical flume with the net model presented by the reference [24], and the simulated results are compared with experimental and CFD results of the reference. Figure 6b presents the comparison results and a good fitting is observed, further confirming the reliability of the numerical model used in this study.

Table 5. Three models with different mesh quality.

Type	Mesh Level of the Net	Mesh Level of the Area within 0.15 m around the Net
Coarse	4	3
Medium	5	4
Fine	6	5

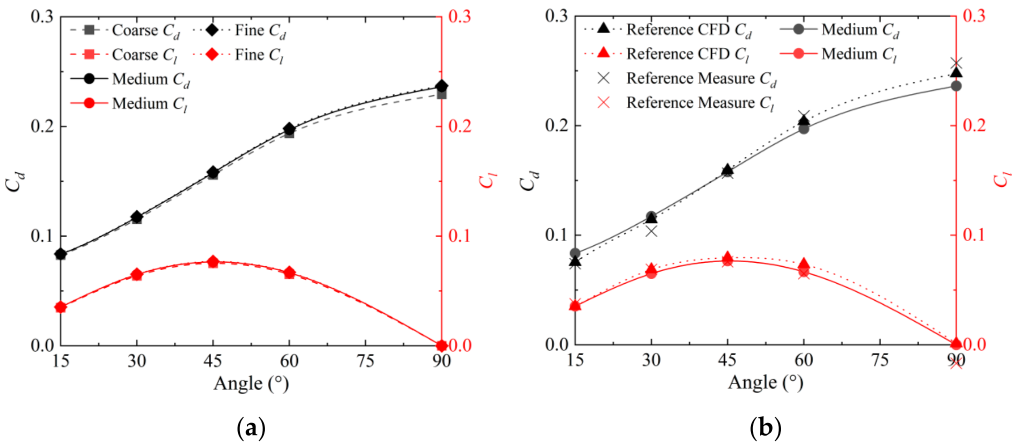

Figure 6. Mesh convergence analysis and model validation. (**a**) Comparison of three types of mesh. (**b**) Comparison between the measured, CFD-calculated values in reference [24] and present results.

3.3. Darcy–Forchheimer Coefficients of the Planar Net

In this study, Darcy–Forchheimer coefficients are crucially used to characterize the porous media model, which is determined using the fitting toolbox embedded in MATLAB-2021. The least absolute normalized error (*LANE*) function is adopted to obtain the Darcy–Forchheimer coefficients for yielding more accurate results [24], which is given as:

$$LANE = \frac{1}{N}\sum_{1}^{N}\left|\frac{F_d - D_{measured}}{D_{measured}}\right| + \frac{1}{M}\sum_{1}^{M}\left|\frac{F_l - L_{measured}}{L_{measured}}\right| \tag{19}$$

where $D_{measured}$ and $L_{measured}$ are the experimentally measured drag and lift force, respectively; N and M are the corresponding number of drag and lift data groups, respectively.

The drag and lift coefficients of the UHMWPE planar net are calculated by the following formulas:

$$C_d = \frac{D}{0.5\rho u_0^2 A} \quad (20)$$

$$C_l = \frac{L}{0.5\rho u_0^2 A} \quad (21)$$

where D is the drag force; L is the lift force; C_d and C_l are the drag and lift coefficients of the planar net, respectively.

Since the accuracy of the experimental data for the attack angles of 0° and 15° is questionable, the associated drag and lift force values are excluded from the fitting process [25,26]. Particularly, $r_0 = 1 - r_n C_{d,\ measured}$ is adopted as the initial input value of the reduction factor of velocity within the porous media (r), where $C_{d,\ measured}$ is the experimental drag coefficient of the net. The obtained Darcy–Forchheimer coefficients are employed in the porous media module of OpenFOAM to calculate the hydrodynamic coefficients of the net, which are then compared to the experimental data. In cases where the error is significant, the reduction factor of velocity within the porous media (r) is determined by extracting the average velocity within the net model and put it back into MATLAB's fitting toolbox to get the new Darcy–Forchheimer coefficients. The fitting process continues until the residual reaches a value less than 0.01, at which point the final Darcy–Forchheimer coefficients are obtained and summarized in Table 6.

Table 6. Darcy–Forchheimer coefficients of the planar net obtained by fitting.

Method	D_n (m^{-2})	D_t (m^{-2})	C_n (m^{-1})	C_t (m^{-1})
LANE	700,257.49	588,789.88	11.988205	1.687423
LSM	740,500.31	714,711.92	11.954160	1.456235×10^{-6}

Moreover, the Darcy–Forchheimer coefficients are also fitted through least square method (*LSM*) [31], as listed in Table 6. The corresponding computational results are shown in Figure 7 for the case of incoming velocity u_0 = 1.0 m/s. In comparison with the measured data, the average deviations for the drag and lift coefficients obtained by *LANE* and *LSM* are 14.14% and 14.33%, respectively, showing the same precision and verifying the accuracy of the fitting method LANE adopted in this study.

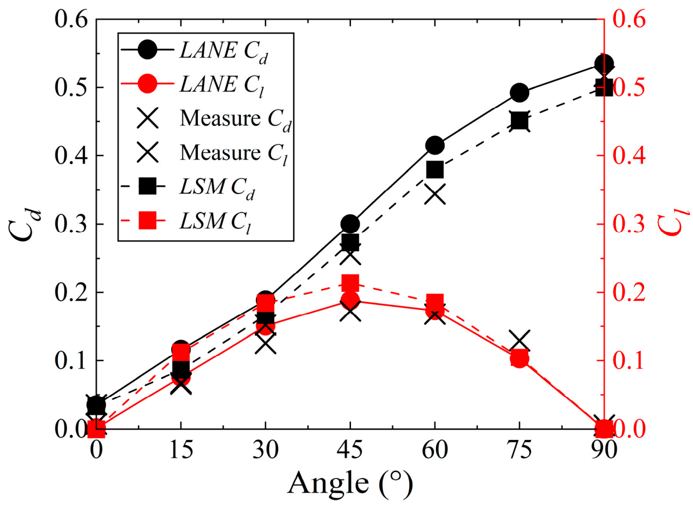

Figure 7. Comparison of the hydrodynamic coefficients for the net obtained from CFD (numerical computation based on the Darcy–Forchheimer coefficients fitted by *LANE* and *LSM*) and measured data. (u_0 = 1.0 m/s).

The comparison is conducted between the hydrodynamic coefficients (C_d and C_l) obtained through CFD simulations and experimental values, as illustrated in Figure 8. The deviation between them is determined to be 15.41% by calculating the least absolute normalized error of the planar net. However, certain values such as the drag and lift forces for 0° and 15° attack angles, as well as the lift values for 90° attack angles, are excluded during the calculation due to the inaccuracy of experimental measurements [25,26]. Generally, good fittings between the numerical results and experimental data are obtained; see Figure 8.

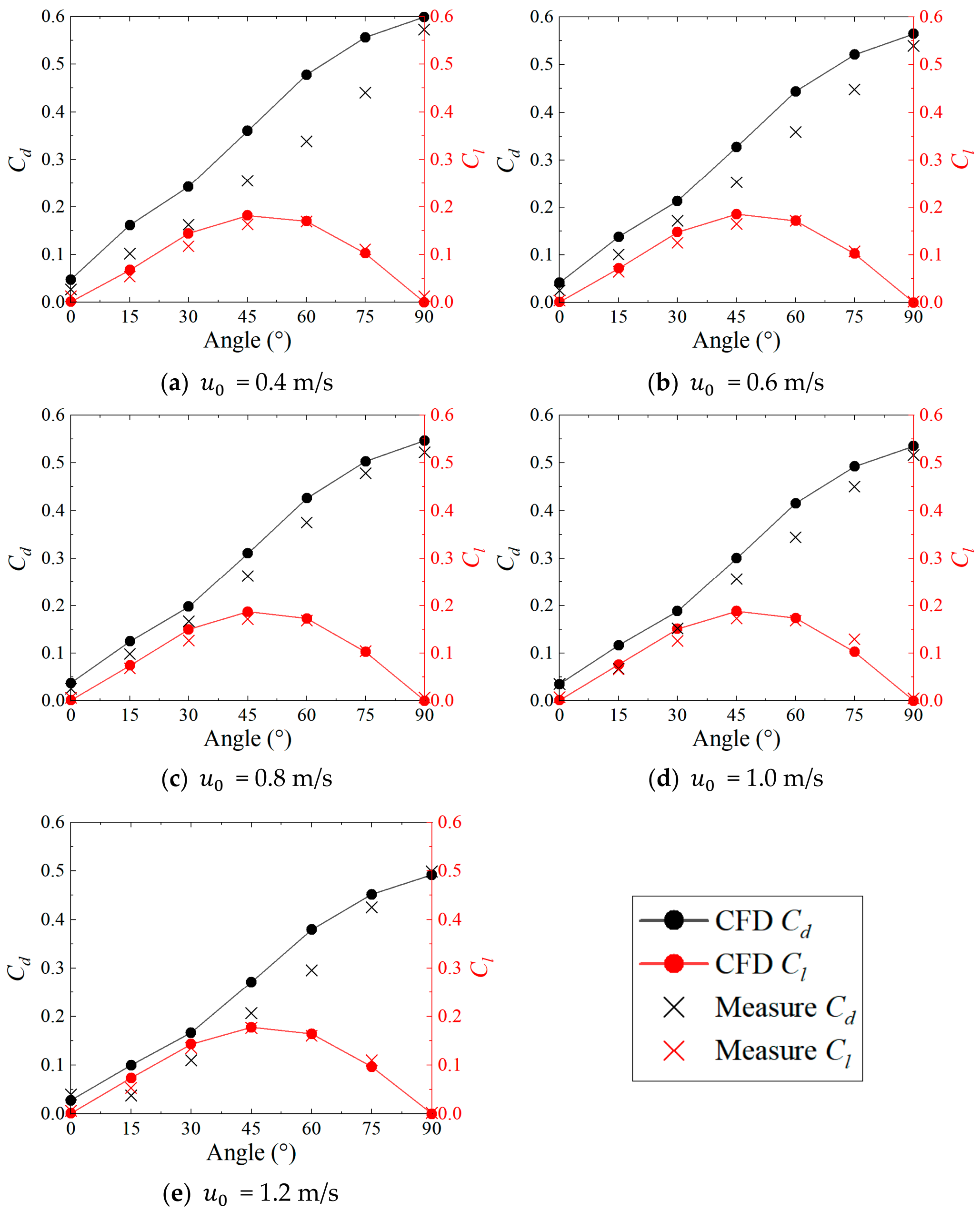

Figure 8. Comparison of the hydrodynamic coefficients for the net between the CFD calculated results and the experimental measurements.

4. Establishing and Validating the Numerical Model for the Cylindrical Cage

After the Darcy–Forchheimer coefficients are determined, the planar net is employed to construct the cylindrical cage for the flow field characteristic analysis.

In this study, the numerical model, consisting of a flume with dimensions of 240 m in length, 80 m in width, and a water depth of 20 m, as well as the cage with the diameter (d) and height (h) of 16 m and 10 m, respectively, is determined by referring to a previous study [26], as illustrated in Figure 9. Moreover, the upper surface of the cage is flush with the upper boundary of the numerical flume, i.e., liquid level, whose center point is the origin of the global coordinate system for the numerical model. The boundary conditions and solver settings used in this section are consistent with those described in Section 3.2, and the inlet turbulence quantities k and ε are tabulated in Table 7.

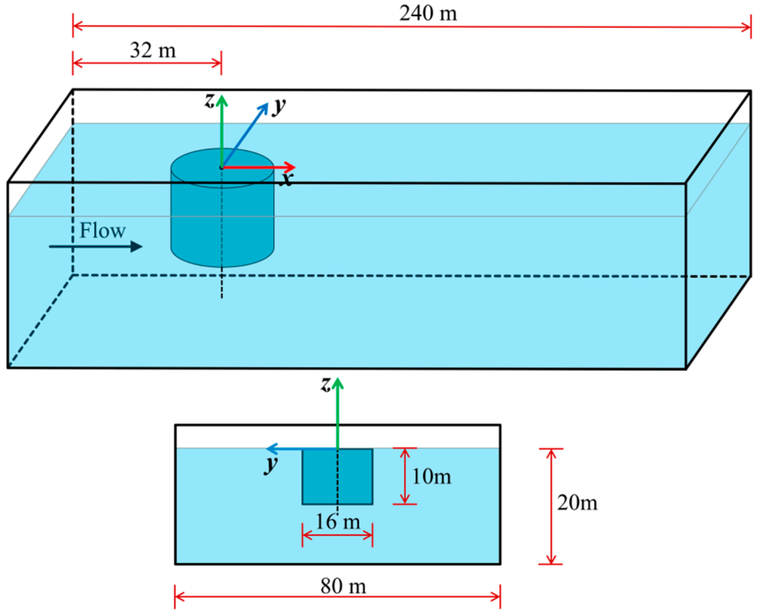

Figure 9. Sketch of the numerical model for the cylindrical cage.

Table 7. Inlet turbulence quantities k and ε of the numerical model for cage.

Velocity (m/s)	k (m^{-2}/s^{-2})	ε (m^{-2}/s^{-3})
0.2	3.05384×10^{-5}	1.23795×10^{-8}
0.6	2.08837×10^{-4}	2.21384×10^{-7}
1.0	5.10556×10^{-4}	8.46252×10^{-7}
1.4	9.19958×10^{-4}	2.04685×10^{-6}

The cylindrical cage is divided into 16 planar nets circumferentially, as well as an additional bottom net, where the parameters of each planar net for different attack angles are identical to those specified in Section 3. To simplify the numerical model, we assume that the cylindrical cage is rigid and only consider its effect on the flow field, which is reasonable in view of current cages made of UHMWPE, viz., “Deep Blue I”, “Long Whale I”, etc.

4.1. Mesh Grids and Convergence Analysis

The method used to generate the mesh is the same as in Section 3.3. Herein, to ensure the accuracy and efficiency of the numerical simulation, three types of mesh are generated to perform mesh convergence analysis, where the net mesh with a thickness of 0.05 m is divided into 1, 3 and 5 layers along the thickness direction, respectively. The comparison results for the drag force obtained by different mesh strategies are presented in Table 8, and a negligible discrepancy is observed for the Medium and Fine cases; hence, the Medium type is employed in the following numerical simulation.

Table 8. Comparison results of mesh convergence analysis (u_0 = 1.0 m/s).

Type	Layers	Drag (N)	Relative Error
Coarse	1	58,262.52	6.87%
Medium	3	62,562.12	0.59%
Fine	5	62,193.45	0.00%

4.2. Validation of Numerical Models

The accuracy of the model is verified by comparing the minimum reduction factor of the flow velocity behind the last cage downstream obtained from the CFD numerical simulation and empirical formulas. Therefore, the velocity is normalized to better reveal the variation trend, viz., the reduction factor of the flow velocity at any position, as following:

$$U_r = \frac{u}{u_0} \tag{22}$$

By combining previous theories and experiments, Aarsnes et al. [6] proposed that the flow velocity will decline after the water flows through the cage, with the degree of reduction as the following expression:

$$U_{r,min} = \prod_{i=1}^{n_c} r_i \tag{23}$$

$$r_i = 1.0 - 0.46C_d \tag{24}$$

where $U_{r,min}$ is the minimum reduction factor of the flow velocity behind the last cage downstream, reflecting the maximum flow velocity deficit induced by the cage; r_i is the empirical coefficient; n_c is the number of times that the water flows through the cage.

The overall drag coefficient C_d of the cage at u_0 = 1.0 m/s can be obtained as 0.78, and furthermore, r_i = 0.64. The comparison of $U_{r,min}$ derived from CFD numerical simulation and empirical formulas is shown in Figure 10, where a good fitting can be observed, indicating the accuracy of the numerical simulation.

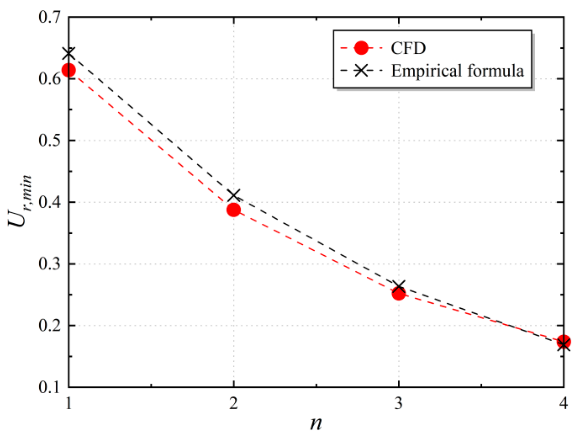

Figure 10. The comparison of CFD numerical simulation and empirical formulas.

5. Numerical Study on the Flow Field of the Cylindrical Cage

5.1. Numerical Simulation of a Single Cylindrical Cage

In this section, numerical simulations are carried out to investigate the internal and external flow fields for a single cylindrical cage, based on the numerical model in Section 4.1. The along-line distribution of velocity, which passes through the geometric center point of the single cylindrical cage, is revealed at different flow velocities as shown in Figure 11, and the detailed analyses are presented in the following.

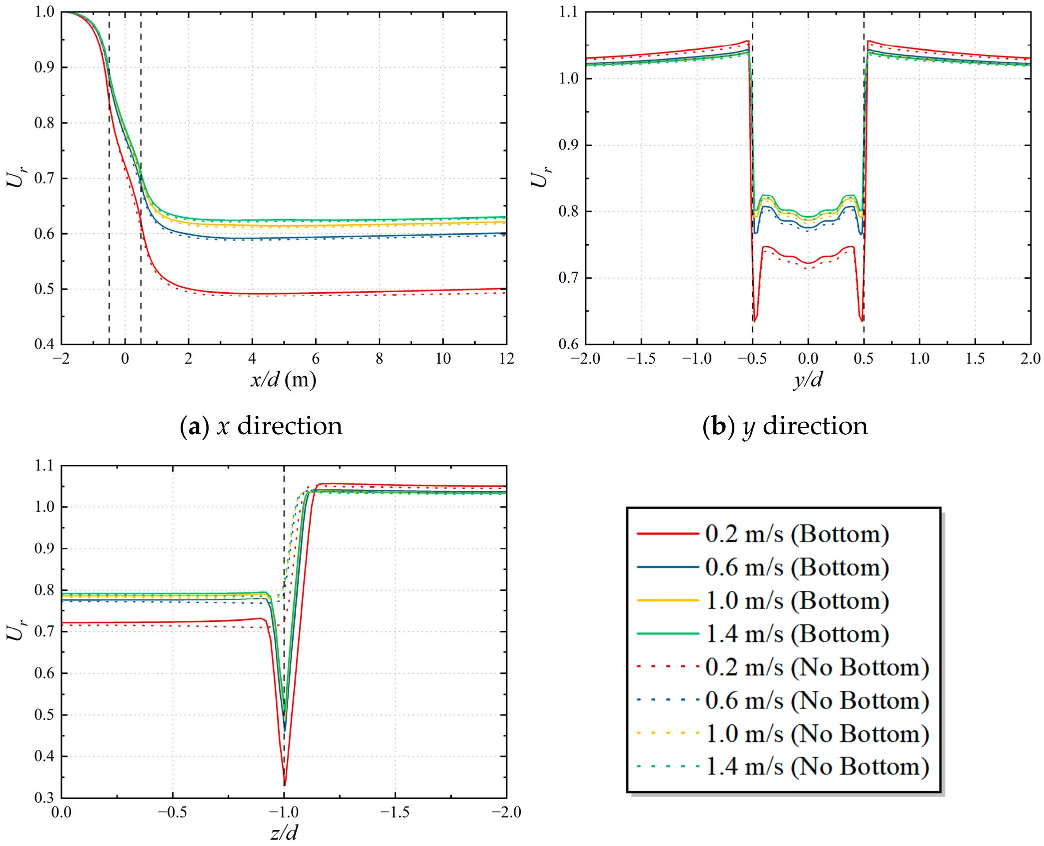

(**a**) x direction (**b**) y direction

(**c**) z direction

Figure 11. Velocity distribution along the line passing through the geometric center point of the single cylindrical cage.

As shown in Figure 11a, along the direction of incoming flow, there are large decelerations in front of and behind, as well as inside the cage, and the flow field gradually stabilizes as it moves away from the cage, suggesting that the cage no longer has a significant shading effect on the flow field. Meanwhile, Figure 11b,c reveal a large deceleration inside the cage, accompanied by an increase in velocity on the bottom and sides of it. It can be seen that the velocity distribution along the z direction displays an abrupt change at z/d, which stems from the effect of the bottom net. Overall, the degree of deceleration diminishes as the velocity increases, while this effect gradually becomes less pronounced with further increase in velocity. In particular, the velocity description of the cylindrical cage shown in Figure 11b is similar to that of solid cylinders [40,41], validating the reliability of the simulation. To illustrate the impact of the bottom net of the cage more clearly, we examined the bottomless single cage model, which was considered in previous numerical studies [42,43]. The comparison reveals minimal differences in the flow field distribution between the bottom and bottomless models, with a maximum percentage difference of 6.77% in the drag (Figure 12); however, the cage with bottom net induces an abrupt change in velocity distribution in the z direction, which is not observed for the bottomless one, as indicated in Figure 11c.

Figure 13 presents the velocity distribution along the line apart from the one passing through the geometric center point of the cage. The velocity distribution along the x and y directions shows minimal variation with changes in the z coordinate, as illustrated in Figure 13a,b. At $z = -8$ m, the velocity distribution in the x direction recovers more rapidly compared with other locations due to the weaker shielding effect of the cage on the flow field at the rear of the cage's bottom. Moreover, the distribution of velocity along the z direction changes weakly for different y coordinate values, as shown in Figure 13c.

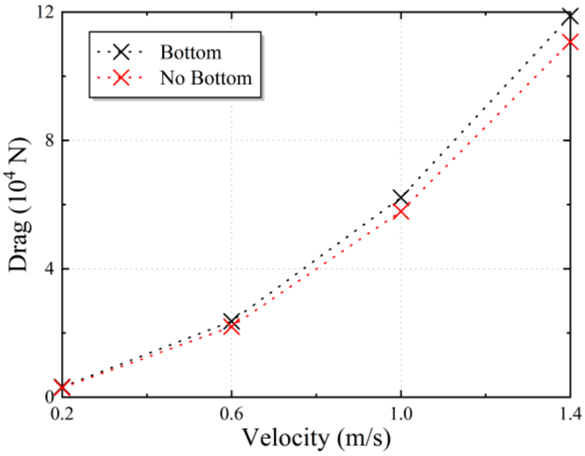

Figure 12. Comparison of the drag force on the cage with and without bottom net.

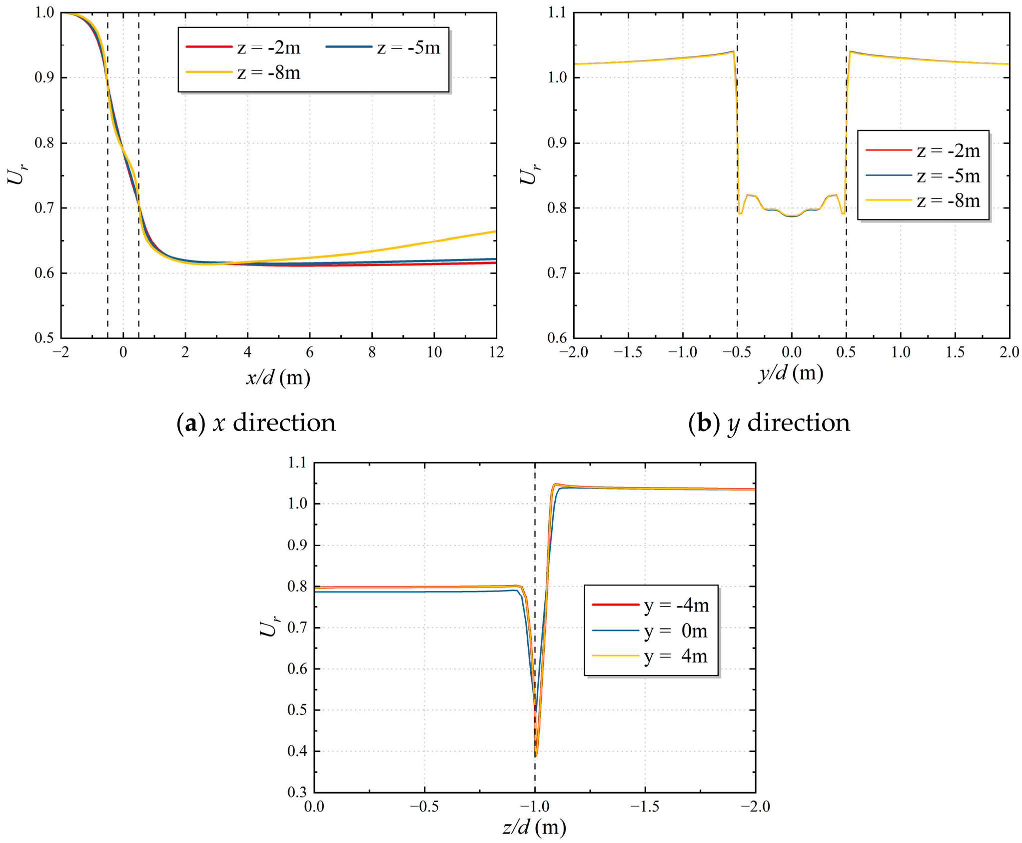

(**a**) x direction (**b**) y direction

(**c**) z direction

Figure 13. Velocity distribution along the line at other locations for the single cylindrical cage (u_0 = 1.0 m/s).

The profile of the flow field at $z/d = -0.5$ is depicted in Figure 14. A significant deceleration in the velocity is observed inside the cage and in a certain area in front of and behind it, consistent with the phenomenon observed in Figure 11. Moreover, an acceleration of flow velocity is present in the flow field surrounding the cage, resulting in a 3% to 10%

increase in velocity, which is due to the obstructive effect of the cage on the flow field increasing the pressure difference at the two sides.

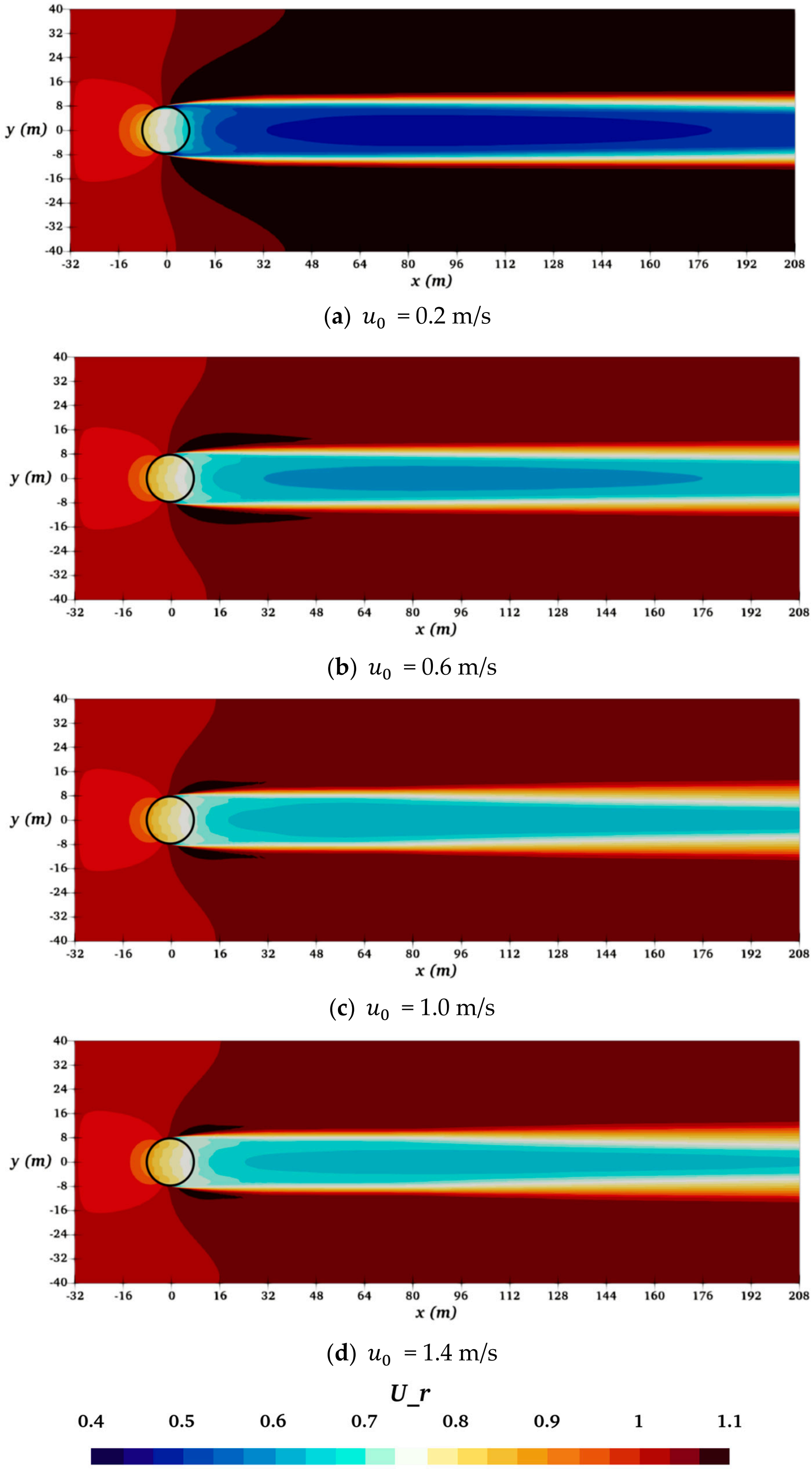

(**a**) u_0 = 0.2 m/s

(**b**) u_0 = 0.6 m/s

(**c**) u_0 = 1.0 m/s

(**d**) u_0 = 1.4 m/s

Figure 14. The profile of the flow field at $z/d = -0.5$.

5.2. Numerical Simulation of Double Cylindrical Cages with Different Spacing

In this section, an additional cage model is set downstream of the single cage model in Section 5.1 with different spacing (L) of 0.5d, 1.0d, 1.5d, and 2.0d, to investigate the effect of different spacing on the flow field.

In terms of the along-line distribution of velocity in the x direction, the downstream deceleration remains consistently high at 62%, with little variation as the spacing is increased, as shown in Figure 15a. In addition, the flow field in the vicinity of the upstream cage remains relatively unchanged, resulting in a deceleration ranging from 11% to 31% regardless of the change in spacing. However, the gradient of deceleration between the cages decreases as the spacing is increased, induced by the deceleration zone elongating even though the total deceleration effect remains constant. As depicted in Figure 15b,c, the along-line distribution of velocity in the y direction and z direction is minimally affected by the change in spacing for the downstream cylindrical cage.

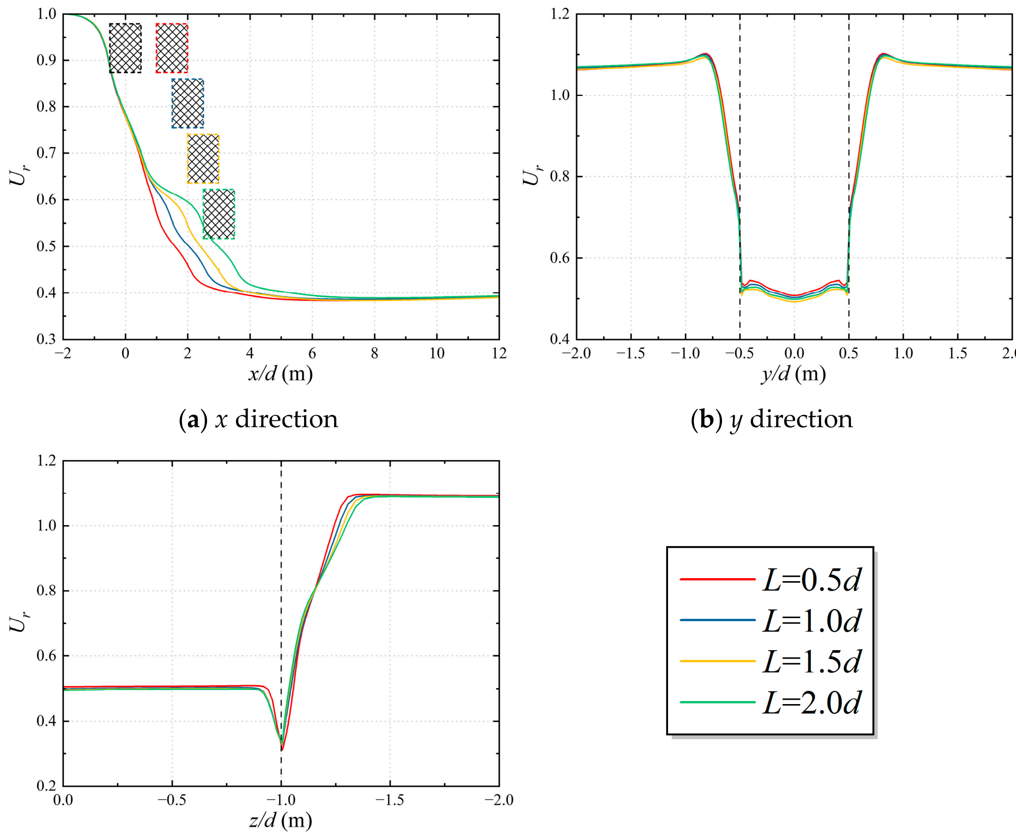

(**a**) x direction (**b**) y direction

(**c**) z direction

Figure 15. Velocity distribution along the line passing through the geometric center point of the most downstream cylindrical cage for double cylindrical cages (u_0 = 1.0 m/s).

It is evident from Figure 16 that the velocity distribution of the flow field within the two cages and behind the downstream cage is minimally affected by the variation in spacing, which is consistent with the observation described in Figure 15. Moreover, the gradient of deceleration between two cages can also be clearly noticed to decrease with the elongation of the spacing.

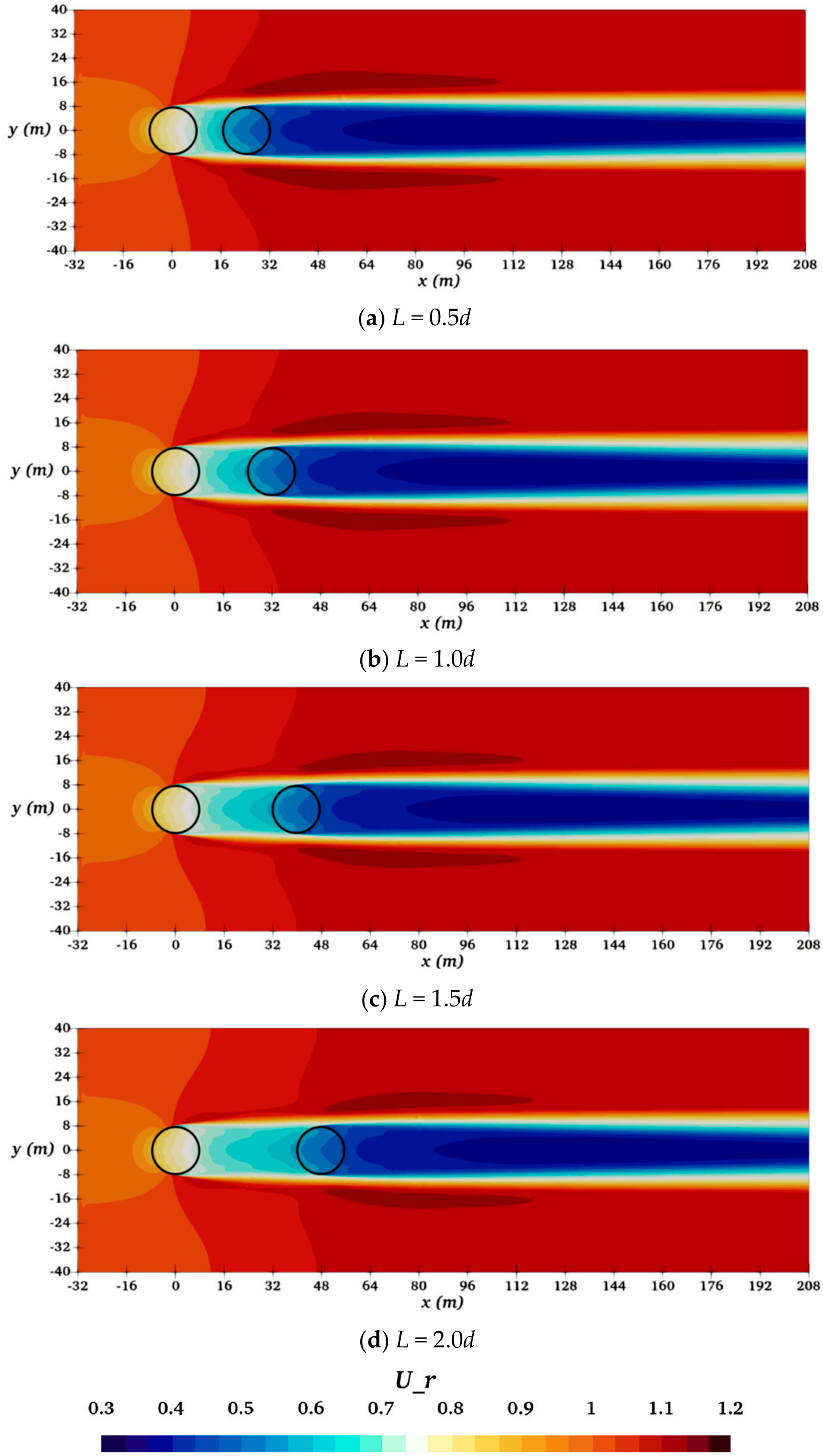

Figure 16. The profile of the flow field at $z/d = -0.5$ for double cylindrical cages ($u_0 = 1.0$ m/s).

5.3. Numerical Simulation of Multiple Cylindrical Cages with Same Spacing

In this section, based on the numerical model in Section 5.1, multiple cages are installed downstream with the same spacing ($L = 1.5d$) to study the effect of the number of cages (n) on the flow field, where $n = 1, 2, 3$ and 4.

Figure 17a illustrates that the downstream cages have a superimposed effect on the deceleration of the flow field, while insignificant influence is observed on the flow field near the upstream cages. As can be seen from Figure 17b,c, the velocity tends to be gentle when the region moves away from the most downstream cage along the y and z directions. The velocity in the gentle zone is greater than the incoming flow velocity, which is the same as that depicted in Figure 11b,c with the phenomenon. Moreover, the degree of increase in velocity at the aforementioned gentle zone rises with the increasing number of cages (n), and the degrees of increase for $n = 1, 2, 3$ and 4 are 2.41%, 7.39%, 11.28% and 13.86%, respectively, while the distance from the deceleration zone to the gentle zone is lengthened. It can also be noted from Figure 17c that the abrupt change in the velocity distribution of the most downstream cage in the z direction at the bottom net becomes less apparent as the number of cages (n) rises, due to the limited minimum velocity and the effect of excessive deceleration. Overall, combining the variation trends in Figure 17, an increase in the number of cages (n) causes a significant decrease in the most downstream flow velocity, and the superimposed deceleration due to each additional cage gradually decreases.

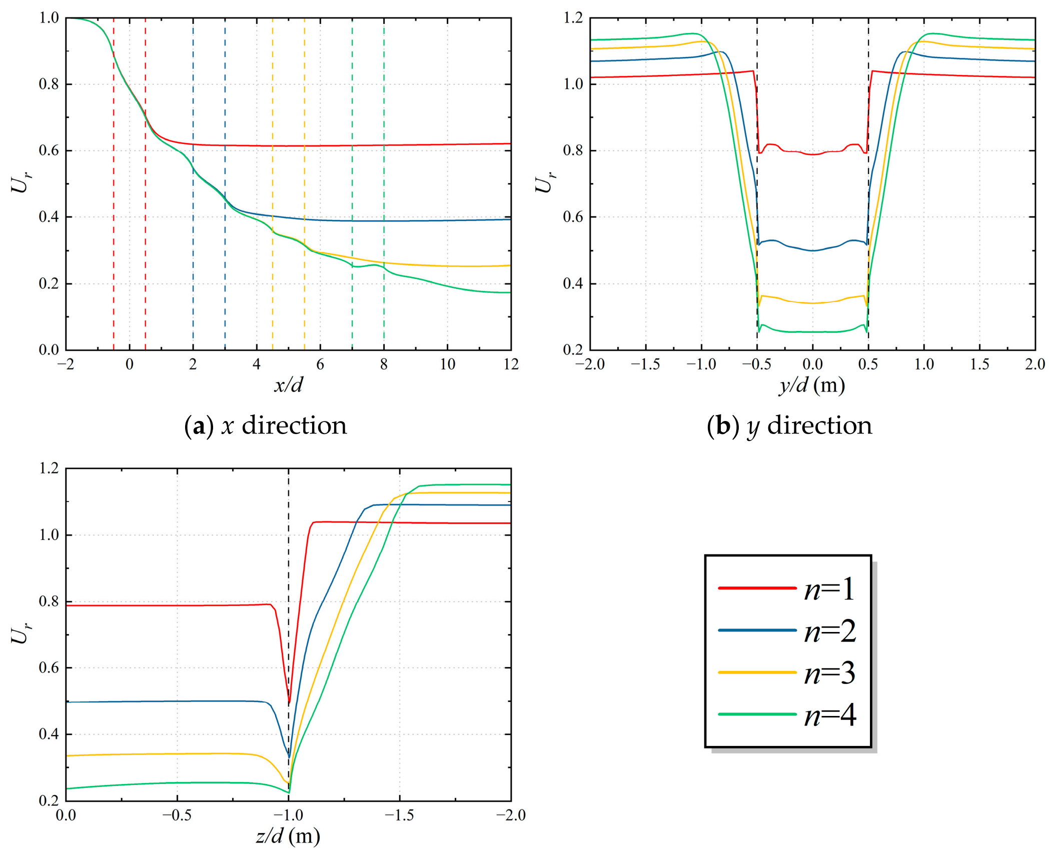

(**a**) x direction (**b**) y direction

(**c**) z direction

Figure 17. Velocity distribution along the line passing through the geometric center point of the most downstream cylindrical cage for multiple cylindrical cages ($u_0 = 1.0$ m/s).

The flow field of multiple cages is presented in Figure 18, in which it can be explicitly seen that the downstream cages have almost no effect on the flow field near the upstream cages, i.e., the phenomenon described earlier depending on Figure 17. Moreover, the velocity of the flow field on both sides of the most downstream cage will gradually grow as the number of cages (n) increases. Finally, according to the velocity nephogram, the corresponding deceleration inside the most downstream cage is 0.22, 0.50, 0.66 and 0.75, respectively, for n = 1, 2, 3 and 4.

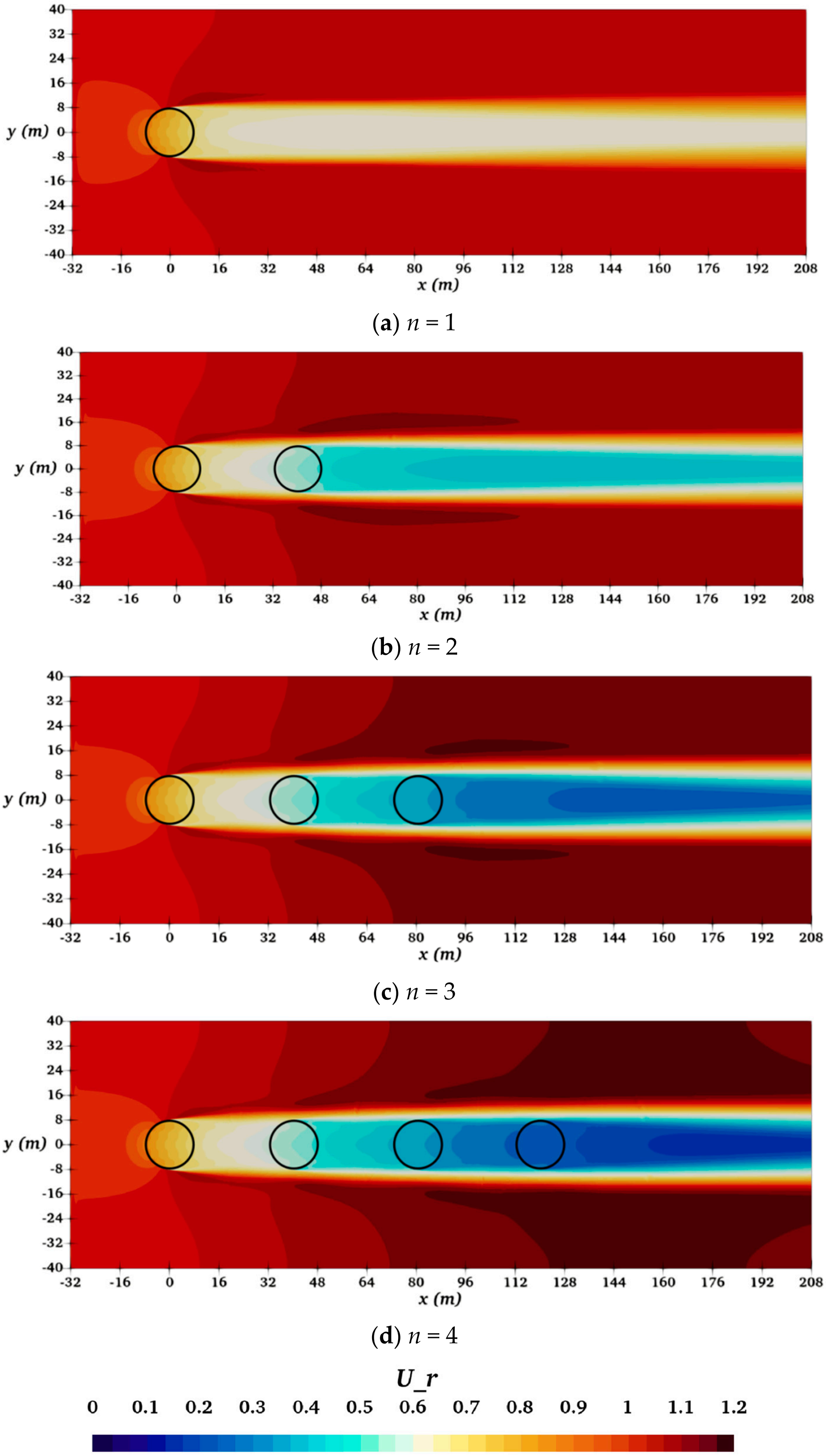

(**a**) $n = 1$

(**b**) $n = 2$

(**c**) $n = 3$

(**d**) $n = 4$

Figure 18. The profile of the flow field at $z/d = -0.5$ for multiple cylindrical cages (u_0 = 1.0 m/s).

6. Conclusions

In this study, the surrounding flow field of the UHMWPE cage is investigated numerically by using the CFD method and modeling the net as a porous media model. The following conclusions are obtained:

(1) The UHMWPE planar net is well simulated by the porous media model with a solidity of 0.13, and the simulation results of hydrodynamic characteristics are in excellent agreement, where the Darcy–Forchheimer coefficients are fitted by experimental data.

(2) The UHMWPE cylindrical cage is divided into 16 planar nets circumferentially as well as an additional bottom net, and the internal and external flow fields are investigated in detail. For a single cylindrical cage, the degree of deceleration diminishes as the velocity increases, while this effect gradually becomes less pronounced with further increase in velocity. Meanwhile, an acceleration of flow velocity exists on the bottom and sides of the cage, with an increase of 3% to 10%. In addition, the weaker shielding effect of the cage on the flow field at the rear of the cage's bottom is noted, which allows the local flow velocity to recover rapidly. Furthermore, the cage with bottom net induces an abrupt change of velocity distribution in the z direction, while this is not observed for the bottomless one.

(3) With UHMWPE double cylindrical cages, the effect on the flow field is hardly influenced by changing spacing, where the downstream deceleration induced by double cages is 62%, and a decrease in the gradient of deceleration between two cages can be noticed with increasing spacing. Upon the number of cages further increasing, the deceleration presented by multiple cages downstream is enhanced, and the degree of increase in velocity around the cage rises with the number of cages (n) increasing, which is 2.41%, 7.39%, 11.28% and 13.86% for n = 1, 2, 3 and 4, respectively. In addition, the additional downstream cages have little effect on the flow field in the vicinity of the upstream cages. Finally, the corresponding deceleration inside the downstream cage is 0.22, 0.50, 0.66 and 0.75, respectively, for n = 1, 2, 3 and 4.

Author Contributions: Conceptualization, Y.H., H.Z., W.S., C.B. and X.L.; methodology, Y.H.; software, Y.H.; validation, Y.H. and H.Z.; formal analysis, Y.H.; investigation, Y.H. and H.Z.; data curation, Y.H.; writing—original draft preparation, Y.H.; writing—review and editing, H.Z., W.S. and X.L.; supervision, H.Z., W.S., C.B. and X.L.; project administration, W.S. and C.B.; funding acquisition, X.L. All authors have read and agreed to the published version of the manuscript.

Funding: This research work was financially supported by the National Natural Science Foundation of China (Grant No. 51939002) and the Fundamental Research Funds for the Central Universities (Grant No. DUT22RC(3)069).

Institutional Review Board Statement: Not applicable.

Informed Consent Statement: Not applicable.

Data Availability Statement: Not applicable.

Conflicts of Interest: The authors declare no conflict of interest.

References

1. Albrektsen, S.; Kortet, R.; Skov, P.V.; Ytteborg, E.; Gitlesen, S.; Kleinegris, D.; Mydland, L.T.; Hansen, J.Ø.; Lock, E.J.; Mørkøre, T.; et al. Future feed resources in sustainable salmonid production: A review. *Rev. Aquac.* **2022**, *14*, 1790–1812. [CrossRef]
2. Araujo, G.S.; Silva, J.W.A.D.; Cotas, J.; Pereira, L. Fish farming techniques: Current situation and trends. *J. Mar. Sci. Eng.* **2022**, *10*, 1598. [CrossRef]
3. Dong, S.L.; Dong, Y.W.; Cao, L.; Verreth, J.; Olsen, Y.; Liu, W.J.; Fang, Q.Z.; Zhou, Y.G.; Li, L.; Li, J.Y.; et al. Optimization of aquaculture sustainability through ecological intensification in china. *Rev. Aquac.* **2022**, *14*, 1249–1259. [CrossRef]
4. Ren, Z.; Zhen, X.; Jiang, Z.; Gao, Z.; Li, Y.; Shi, W. Underactuated control and analysis of single blade installation using a jackup installation vessel and active tugger line force control. *Mar. Struct.* **2023**, *88*, 103338. [CrossRef]
5. Zhao, Y.X.; Zhang, J.H.; Liu, Y.; Sun, K.; Zhang, C.; Wu, W.G.; Teng, F. Numerical assessment of the environmental impacts of deep sea cage culture in the yellow sea, china. *Sci. Total Environ.* **2020**, *706*, 135752. [CrossRef]

6. Aarsnes, J.V.; Rudi, H.; Løland, G. Current forces on cage, net deflection. In Proceedings of the Engineering for Offshore Fish Farming A Conference Organised by the Institution of Civil Engineers, UK, Glasgow, 17–18 October 1990.
7. Guo, Y.C.; Mohapatra, S.C.; Guedes Soares, C. Review of developments in porous membranes and net-type structures for breakwaters and fish cages. *Ocean Eng.* **2020**, *200*, 107027. [CrossRef]
8. Klebert, P.; Lader, P.; Gansel, L.; Oppedal, F. Hydrodynamic interactions on net panel and aquaculture fish cages: A review. *Ocean Eng.* **2013**, *58*, 260–274. [CrossRef]
9. Zhan, J.M.; Jia, X.P.; Li, Y.S.; Sun, M.G.; Guo, G.X.; Hu, Y.Z. Analytical and experimental investigation of drag on nets of fish cages. *Aquac. Eng.* **2006**, *35*, 91–101. [CrossRef]
10. Løland, G. Current forces on, and water flow through and around, floating fish farms. *Aquac. Int.* **1993**, *1*, 72–89. [CrossRef]
11. Tauti, M. The force acting on the plane net in motion through the water. *Nippon Suisan Gakkaishi* **1934**, *3*, 1–4. [CrossRef]
12. Bi, C.W.; Zhao, Y.P.; Dong, G.H.; Xu, T.J.; Gui, F.K. Experimental investigation of the reduction in flow velocity downstream from a fishing net. *Aquac. Eng.* **2013**, *57*, 71–81. [CrossRef]
13. Bi, C.W.; Zhao, Y.P.; Dong, G.H.; Wu, Z.M.; Zhang, Y.; Xu, T.J. Drag on and flow through the hydroid-fouled nets in currents. *Ocean Eng.* **2018**, *161*, 195–204. [CrossRef]
14. Gansel, L.C.; McClimans, T.A.; Myrhaug, D. The effects of fish cages on ambient currents. *J. Offshore Mech. Arct. Eng. Trans. ASME* **2012**, *134*, 11303. [CrossRef]
15. Joshi, K.; Bhattacharya, S. Large-eddy simulation of the effect of distributed plasma forcing on the wake of a circular cylinder. *Comput. Fluids* **2019**, *193*, 104295. [CrossRef]
16. Joshi, K.; Latrobe, B.; Bhattacharya, S. Altering the wake dynamics of a circular cylinder with harmonic forcing. *Phys. Fluids* **2023**, *35*, 65139. [CrossRef]
17. Zhao, Y.P.; Bi, C.W.; Chen, C.P.; Li, Y.C.; Dong, G.H. Experimental study on flow velocity and mooring loads for multiple net cages in steady current. *Aquac. Eng.* **2015**, *67*, 24–31. [CrossRef]
18. Plew, D.R.; Klebert, P.; Rosten, T.W.; Aspaas, S.; Birkevold, J. Changes to flow and turbulence caused by different concentrations of fish in a circular tank. *J. Hydraul. Res.* **2015**, *53*, 364–383. [CrossRef]
19. Bi, C.W.; Zhao, Y.P.; Dong, G.H. Experimental study on the effects of farmed fish on the hydrodynamic characteristics of the net cage. *Aquaculture* **2020**, *524*, 735239. [CrossRef]
20. Park, S.; Zhou, J.X.; Dong, S.C.; Li, Q.; Yoshida, T.; Kitazawa, D. Characteristics of the flow field inside and around a square fish cage considering the circular swimming pattern of a farmed fish school: Laboratory experiments and field observations. *Ocean Eng.* **2022**, *261*, 112097. [CrossRef]
21. Klebert, P.; Su, B. Turbulence and flow field alterations inside a fish sea cage and its wake. *Appl. Ocean Res.* **2020**, *98*, 102113. [CrossRef]
22. Gansel, L.C.; Rackebrandt, S.; Oppedal, F.; McClimans, T.A. Flow fields inside stocked fish cages and the near environment. *J. Offshore Mech. Arct. Eng. Trans. ASME* **2014**, *136*, 31201. [CrossRef]
23. Dong, S.C.; Park, S.; Kitazawa, D.; Zhou, J.X.; Yoshida, T.; Li, Q. Model tests and full-scale sea trials for drag force and deformation of a marine aquaculture net cage. *Ocean Eng.* **2021**, *240*, 109941. [CrossRef]
24. Patursson, Ø.; Swift, M.R.; Tsukrov, I.; Simonsen, K.; Baldwin, K.; Fredriksson, D.W.; Celikkol, B. Development of a porous media model with application to flow through and around a net panel. *Ocean Eng.* **2010**, *37*, 314–324. [CrossRef]
25. Zhao, Y.P.; Bi, C.W.; Dong, G.H.; Gui, F.K.; Cui, Y.; Guan, C.T.; Xu, T.J. Numerical simulation of the flow around fishing plane nets using the porous media model. *Ocean Eng.* **2013**, *62*, 25–37. [CrossRef]
26. Zhao, Y.P.; Bi, C.W.; Dong, G.H.; Gui, F.K.; Cui, Y.; Xu, T.J. Numerical simulation of the flow field inside and around gravity cages. *Aquac. Eng.* **2013**, *52*, 1–13. [CrossRef]
27. Bi, C.W.; Zhao, Y.P.; Dong, G.H.; Cui, Y.; Gui, F.K. Experimental and numerical investigation on the damping effect of net cages in waves. *J. Fluids Struct.* **2015**, *55*, 122–138. [CrossRef]
28. Bi, C.W.; Zhao, Y.P.; Dong, G.H.; Xu, T.J.; Gui, F.K. Numerical study on wave attenuation inside and around a square array of biofouled net cages. *Aquac. Eng.* **2017**, *78*, 180–189. [CrossRef]
29. Bi, C.W.; Zhao, Y.P.; Dong, G.H.; Zheng, Y.N.; Gui, F.K. A numerical analysis on the hydrodynamic characteristics of net cages using coupled fluid-structure interaction model. *Aquac. Eng.* **2014**, *59*, 1–12. [CrossRef]
30. Chen, H.; Christensen, E.D. Development of a numerical model for fluid-structure interaction analysis of flow through and around an aquaculture net cage. *Ocean Eng.* **2017**, *142*, 597–615. [CrossRef]
31. Chen, H.; Christensen, E.D. Investigations on the porous resistance coefficients for fishing net structures. *J. Fluids Struct.* **2016**, *65*, 76–107. [CrossRef]
32. Liu, H.F.; Bi, C.W.; Xu, Z.J.; Zhao, Y.P. Hydrodynamic assessment of a semi-submersible aquaculture platform in uniform fluid environment. *Ocean Eng.* **2021**, *237*, 109656. [CrossRef]
33. Liu, H.F.; Bi, C.; Xu, Z.; Zhao, Y.P. Numerical study on the flow environment for a novel design of net cage with a shielding device. *Ocean Eng.* **2022**, *243*, 110345. [CrossRef]
34. Li, N.; Shi, W.; Han, X.; Li, X.; Verma, A.S.; Liu, C.G. Dynamic analysis of an integrated offshore structure comprising a jacket-supported offshore wind turbine and aquaculture steel cage. *Ocean Eng.* **2023**, *274*, 114059. [CrossRef]
35. Kartal, G.E.; Sariisik, A.M. Modifying of uhmwpe fishing nets with layer-by-layer deposition method for antifouling properties. *J. Coat. Technol. Res.* **2021**, *18*, 163–171. [CrossRef]
36. Forchheimer, P. Wasserbewegung durch boden. *Zeitschrift des Vereines Deutscher Ingenieure* **1901**, *45*, 1782–1788.

37. Shih, T.H.; Liou, W.W.; Shabbir, A.; Yang, Z.; Jiang, Z. A new k-e eddy viscosity model for high reynolds number turbulent flows. *Comput. Fluids* **1995**, *24*, 227–238. [CrossRef]
38. Wang, S.G. Study on Hydrodynamic Characteristics of Uhmwpe Plane Netting Nettings and Numerical Simulation. Master's Thesis, Shanghai Ocean University, Shanghai, China, 2020.
39. Fredheim, A. Current Forces on net Structure. Ph.D. Thesis, Norwegian University of Science and Technology (NTNU), Trondheim, Norway, 2005.
40. Ahmed, A.; Bhattacharya, S.; Ahmed, H.; Moore, M.H. On the cylinder wake subjected to in-phase and out-of-phase periodic forcing. *Int. J. Heat Fluid Flow* **2020**, *86*, 108708. [CrossRef]
41. Bhattacharya, S.; Ahmed, A. Effect of sinusoidal forcing on the wake of a circular cylinder. In Proceedings of the 48th AIAA Aerospace Sciences Meeting Including the New Horizons Forum and Aerospace Exposition 2010, Orlando, FL, USA, 4–7 January 2010.
42. Faltinsen, O.M.; Shen, Y.G. Wave and current effects on floating fish farms. *J. Mar. Sci. Appl.* **2018**, *17*, 284–296. [CrossRef]
43. Kristiansen, T.; Faltinsen, O.M. Modelling of current loads on aquaculture net cages. *J. Fluids Struct.* **2012**, *34*, 218–235. [CrossRef]